

Structural basis for allosteric regulation of human phosphofructokinase-1

Received: 28 March 2024

Accepted: 19 August 2024

Published online: 25 August 2024

Eric M. Lynch¹, Heather Hansen², Lauren Salay¹, Madison Cooper²,
Stepan Timr³, Justin M. Kollman¹✉ & Bradley A. Webb²✉

Phosphofructokinase-1 (PFK1) catalyzes the rate-limiting step of glycolysis, committing glucose to conversion into cellular energy. PFK1 is highly regulated to respond to the changing energy needs of the cell. In bacteria, the structural basis of PFK1 regulation is a textbook example of allostery; molecular signals of low and high cellular energy promote transition between an active R-state and inactive T-state conformation, respectively. Little is known, however, about the structural basis for regulation of eukaryotic PFK1. Here, we determine structures of the human liver isoform of PFK1 (PFKL) in the R- and T-state by cryoEM, providing insight into eukaryotic PFK1 allosteric regulatory mechanisms. The T-state structure reveals conformational differences between the bacterial and eukaryotic enzyme, the mechanisms of allosteric inhibition by ATP binding at multiple sites, and an autoinhibitory role of the C-terminus in stabilizing the T-state. We also determine structures of PFKL filaments that define the mechanism of higher-order assembly and demonstrate that these structures are necessary for higher-order assembly of PFKL in cells.

Glycolysis is an ancient, highly-conserved metabolic pathway for the extraction of energy from sugars. During glycolysis, glucose is metabolized to produce energy in the form of ATP, the essential cofactor NADH, as well as other biosynthetic precursors to support cellular functions. The first committed step of glycolysis is catalyzed by phosphofructokinase-1 (PFK1), which converts fructose 6-phosphate (F6P) to fructose 1,6-bisphosphate (F1,6BP), consuming one molecule of ATP in the process. Given this central role as the gatekeeper of glycolysis, PFK1 is heavily regulated by the energy state of the cell; PFK1 is activated by signals of low cellular energy, such as AMP and ADP, and inhibited by signals of high cellular energy, such as ATP and citrate.

The structural basis for PFK1 regulation is best described for the bacterial enzyme^{1–3}. Bacterial PFK1 is a D2-symmetric homotetramer with four active sites, each formed at an interface between two monomers. The enzyme transitions between an active R-state conformation, promoted by binding to F6P and allosteric activators, and an inactive T-state conformation, observed in the absence of F6P and

upon binding to allosteric inhibitors. The R-state to T-state transition involves a rotation between essentially rigid dimers and rearrangement of active site residues, which together function to disrupt the F6P binding pocket².

The PFK1 catalytic domain architecture is conserved in eukaryotes. However, eukaryotic PFK1 has an additional regulatory domain, which arose from gene duplication, tandem fusion, and evolution of the ancestral prokaryotic catalytic domain^{4–6}. The resulting eukaryotic PFK1 monomer corresponds to the bacterial dimer that rotates as an essentially rigid body during the R- to T-state transition. Generally, eukaryotic PFK1 tetramerizes via its regulatory domains, producing a quaternary structure distinct from that observed for the prokaryotic enzyme^{7,8}. Oligomerization regulates PFKL activity; tetramers with D2 symmetry represent the active form of the enzyme, and allosteric activators promote tetramerization, while allosteric inhibitors promote tetramer disassembly^{7,9–11}. Eukaryotic PFK1 is subject to additional layers of regulation, being regulated by over 20 allosteric

¹Department of Biochemistry, University of Washington, Seattle, WA, USA. ²Department of Biochemistry and Molecular Medicine, West Virginia University, Morgantown, WV, USA. ³Department of Computational Chemistry, J. Heyrovsky Institute of Physical Chemistry, Czech Academy of Sciences, Prague, Czech Republic. ✉e-mail: jkoll@uw.edu; bradley.webb@hsc.wvu.edu

ligands¹², in addition to post-translational modification by phosphorylation, glycosylation, and acetylation^{13–16}. Vertebrates possess three PFK1 isoforms: platelet (PFKP), muscle (PFKM), and liver (PFKL), each with particular catalytic and regulatory properties, as well as tissue-specific expression profiles¹⁷. PFKL forms filamentous polymers *in vitro* and micron-scale puncta in cells¹⁸. However, whether higher-order assembly of PFKL in cells reflects the filament formation observed with purified protein is unclear. Further, the functional role of these higher-order assemblies remains an open question.

Bacterial PFK1 provides a canonical example of the structural basis for allosteric regulation, though little is known about the structural basis for the regulation of the vertebrate enzyme. Existing crystal structures of vertebrate PFK1 in various ligand states all resemble the R-state, suggesting that crystal packing may preferentially select for the R-state conformation^{6–8}.

Here, we determine cryoEM structures of PFKL in the R- and T-state conformations. The conformation of T-state PFKL differs from its bacterial counterpart and other vertebrate PFK1 structures. The T-state conformation of PFKL is stabilized by binding of the C-terminus across the catalytic and regulatory domains, and truncation of the C-terminus disrupts PFKL regulation. We further show that PFKL forms filaments in both the R- and T-state conformations, present cryoEM structures of filaments in both states, and demonstrate that micron-scale, punctate assemblies of PFKL observed in cells are composed of the same filament structures observed *in vitro*.

Results

Structure of human PFKL in the R-state

We determined structures of human PFKL in the presence of substrates ATP and F6P by cryoEM (Fig. 1). 2D classification produced an incompletely separated mixture of short filaments and free tetramers, which we therefore separated by 3D classification and refined independently (Fig. 1a, b, Supplementary Fig. 1). Free tetramers and tetramers within filaments are in the same conformation (Ca RMSD 0.5 Å for superposition of tetramers) (Fig. 1c), such that combining them in a masked, consensus refinement produced the highest resolution tetramer structure (Fig. 1d) (3.1 Å, 3.6 Å, and 2.9 Å resolution was achieved for the free tetramer, filament, and consensus tetramer structures, respectively; Supplementary Fig. 1b). F6P and ADP are bound in the active sites (Fig. 1e), suggesting catalysis and product formation occurred during sample preparation. ADP is bound at two additional sites on each monomer: an activating allosteric site (site 1) present at the interface between the catalytic and regulatory domains—this site was previously shown to bind ADP, AMP, and a variety of small-molecule activators^{6,19}—as well as a second site (site 2) present in the catalytic domain, adjacent to loop 390–400 connecting to the regulatory domain (Fig. 1e). The allosteric sugar-binding site is also occupied—we modeled this ligand as F1,6BP, produced by catalysis of F6P and ATP by PFKL (Fig. 1e). The F6P-bound PFKL structure presented here is in the active R-state conformation, as revealed by comparison to existing prokaryotic and eukaryotic R-state PFK structures (Fig. 1f)^{3,6,8}.

PFKL filaments assemble as stacked tetramers via two separate interfaces (Fig. 1g), as previously described at lower resolution in a negative stain EM reconstruction¹⁸. Although PFKL filaments can adopt distinct straight or bent architectures¹⁸, adjoining tetramers are all related by twofold symmetry, and we, therefore, imposed C2 symmetry on tetramer pairs during 3D refinement (Supplementary Fig. 1a). Interface 1, the largest interface, is on the symmetry axis and is formed by loops containing residues 511–520 and 693–705 of the regulatory domain. The core of the interface is formed by N702–N702 and F700–F700 interactions, with possible additional interactions between R695 and Y514. Interface 2 also involves residues on loop 693–705 of a different PFKL protomer, which inserts into a groove on the surface of the catalytic domain of the adjoining tetramer. Masked local refinement of interface 1 improved the resolution from 3.6 to 3.5 Å (Fig. 1g,

Supplementary Fig. 1a) while twofold symmetry expansion and local refinement of interface 2 failed to improve the EM map in this region. The precise interactions at interface 2 are therefore less well-resolved (Fig. 1g).

Structure of human PFKL in the T-state

We next aimed to determine the structure of PFKL in the inactive T-state and therefore solved cryoEM structures of PFKL in the presence of ATP but without substrate F6P (Fig. 2, Supplementary Fig. 2). We also included F1,6BP in the sample preparation, as we suspected that occupying additional ligand sites might aid in stabilizing the protein for structure determination. We again observed a mixture of tetramers and short filaments by 2D classification, and therefore processed the data as described for the R-state structures; we again found that free tetramers and filament-associated tetramers were in the same conformation (Ca RMSD 0.39 Å), such that a consensus structure combining both achieved the highest resolution (2.9 Å, 3.1 Å, and 2.6 Å resolution was achieved for the free tetramer, filament, and consensus tetramer structures, respectively; Supplementary Fig. 2b). On each monomer, ATP is bound in the active site, site 2, and a third site (site 3) between the catalytic and regulatory domains that does not contain a nucleotide in the R-state, while activating site 1 is not occupied (Fig. 2a). F1,6BP is bound in the allosteric sugar binding site (Fig. 2a).

In the absence of F6P, PFKL adopts the T-state conformation. Compared with the R-state structure, this involves a rotation between monomers forming the catalytic dimer, which functions to disrupt the active sites (Fig. 2b). With bacterial PFK1, the transition from the R- to the T-state conformation involves a 7 degree rotation between essentially rigid dimers around one of the twofold symmetry axes of the tetramer² (Supplementary Fig. 3a). In contrast, the PFKL R- to T-state transition involves a 7 degree rotation between monomers around a different axis, which is not coincident with any of the three twofold PFKL symmetry axes, but instead is between the pseudo twofold axes relating the catalytic and regulatory domains (Supplementary Fig. 3b). Compared with bacterial T-state PFK1, PFKL exhibits a rotation between catalytic domains—around an axis different from that observed for the R- to T-state transition—as well as structural rearrangements in the region around ATP sites 2 and 3 (Supplementary Fig. 3c). Nonetheless, transition to the T-state in both bacterial PFK1 and PFKL has the same functional outcome: the enzyme is inactivated by disruption of the F6P binding pockets, though without affecting ATP binding in the active sites. In the PFKL structure, ATP binding at site 3 is linked to local unfolding of an adjacent α -helix (Fig. 2c). This disrupts the positions of residues R201 and R292, which in the R-state bind to the phosphate of F6P in the active site of the adjoining catalytic domain (Fig. 2c). ATP binding in site 3 therefore appears to be inhibitory, contributing to disruption of the F6P binding pocket and stabilization of the T-state conformation. In existing R-state human PFKP structures, site 3 is occupied by a phosphate ion (Supplementary Fig. 3d), and both phosphate and sulfate ions have been shown to increase PFK1 activity²⁰. Taken together, this suggests that PFKL site 3 may function as both an allosteric activating and inhibitory site. Consistently, a dual activating and inhibitory role for this site has also been demonstrated for the bacterial enzyme, where site 3 is occupied by the allosteric inhibitor phosphoenolpyruvate in the T-state²¹ and the allosteric activator ADP in the R-state³ (Supplementary Fig. 3d).

Notably, rearrangement of active site residue R201 in PFKL differs from bacterial PFK1, where the corresponding residue R162 instead swaps positions with E161 upon F6P binding and transition to the R-state conformation (Supplementary Fig. 3e). The T-state PFKL structure also differs from existing human PFKP crystal structures, which all exhibit overall catalytic domain conformations resembling the R-state, regardless of F6P occupancy^{7,8}. Most of the PFKP structures also have an R-state arrangement of active site residues, with the exception of an ATP-bound structure (PDB: 4XYJ), which exhibits the

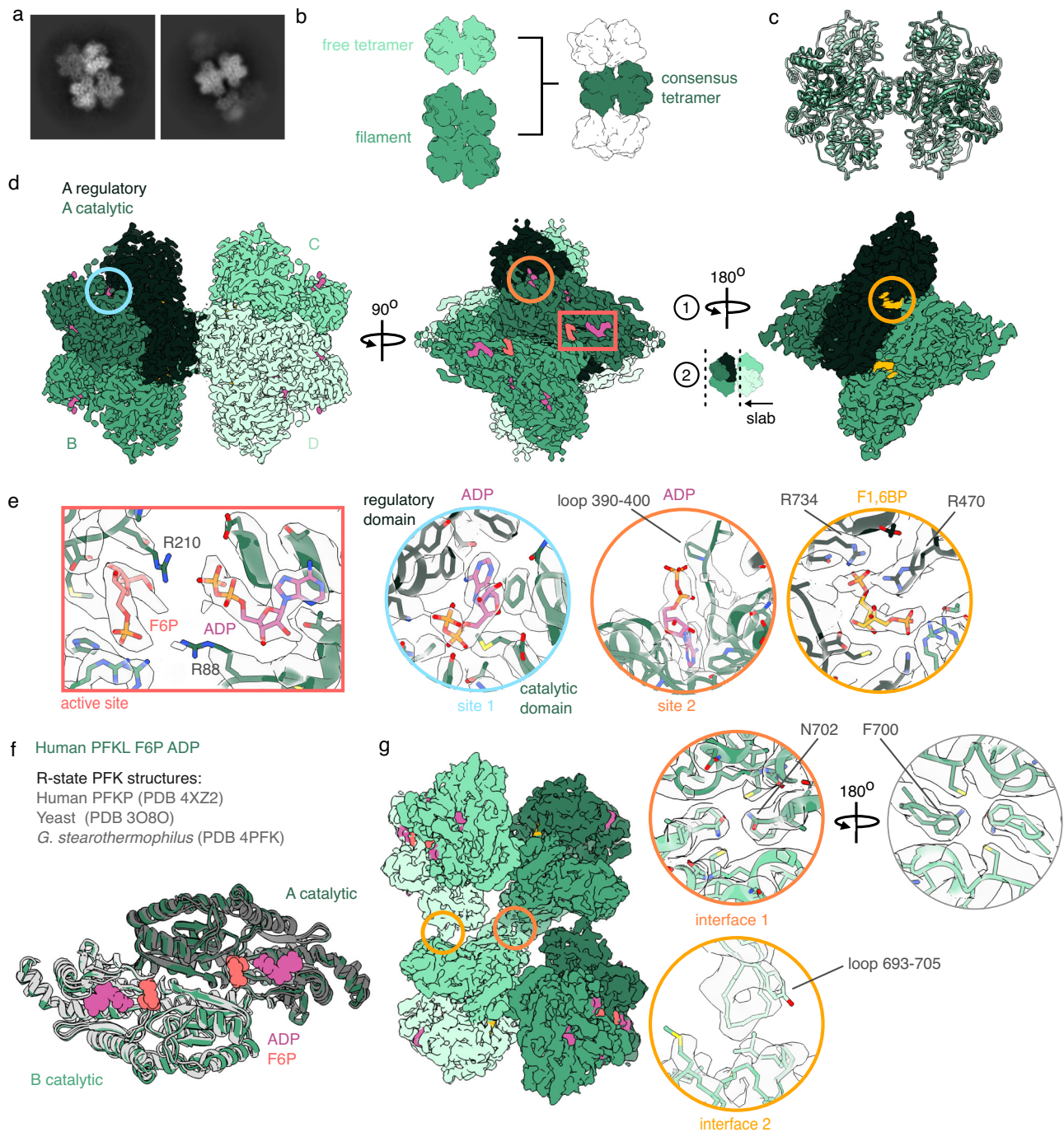


Fig. 1 | cryoEM structures of PFKL tetramers and filaments in the R-state.

a Representative 2D class averages of PFKL in the presence of fructose 6-phosphate (F6P) and ATP. **b** Generalization of the cryoEM processing scheme. Three structures were determined: a free tetramer, a filament, and a consensus tetramer including both free and filament-associated tetramers. **c** Overlay of the three structures outlined in (b) which are in the same conformation. **d** CryoEM structure of the consensus PFKL tetramer, colored by monomer. Monomer A is also colored by domain. **e** Zoomed-in views of the regions indicated in (d) showing the various

ligand-binding sites for ADP, F6P, and fructose 1,6-bisphosphate (F1,6BP). **f** F6P- and ADP-bound PFKL is in the R-state conformation, as revealed by comparison to existing R-state PFK structures. Catalytic domains are shown, with F6P and ADP colored as in panel (e). Structures are aligned on catalytic domain A. **g** CryoEM structure of the R-state PFKL filament, colored by monomer. Circles show zoomed-in views of filament interfaces 1 and 2. Two views of interface 1 are shown, focused on N702 (left) and F700 (right) at the center of the interface.

T-state orientation of R210 (R201 in PFKL) as well as local unfolding similar to that seen adjacent to ATP site 3 in T-state PFKL (Supplementary Fig. 3f).

Transition from the R-state to T-state of PFKL also involves a 7-degree rotation of the regulatory domain towards the catalytic domain within each monomer (Fig. 2d). The rotation compresses the activating site 1, preventing ADP/AMP binding at this site in the T-state

conformation (Fig. 2a). Additionally, the C-terminal tail of PFKL (residues 754–771), which is disordered and not resolved in the R-state structure, is bound in an extended conformation that bridges across the regulatory and catalytic domains in the T-state structure. The tail acts as a kind of strap linking the two domains, suggesting it may function to stabilize the inactive enzyme conformation (Fig. 2d). The conformational changes between the T- and R-states also result in a

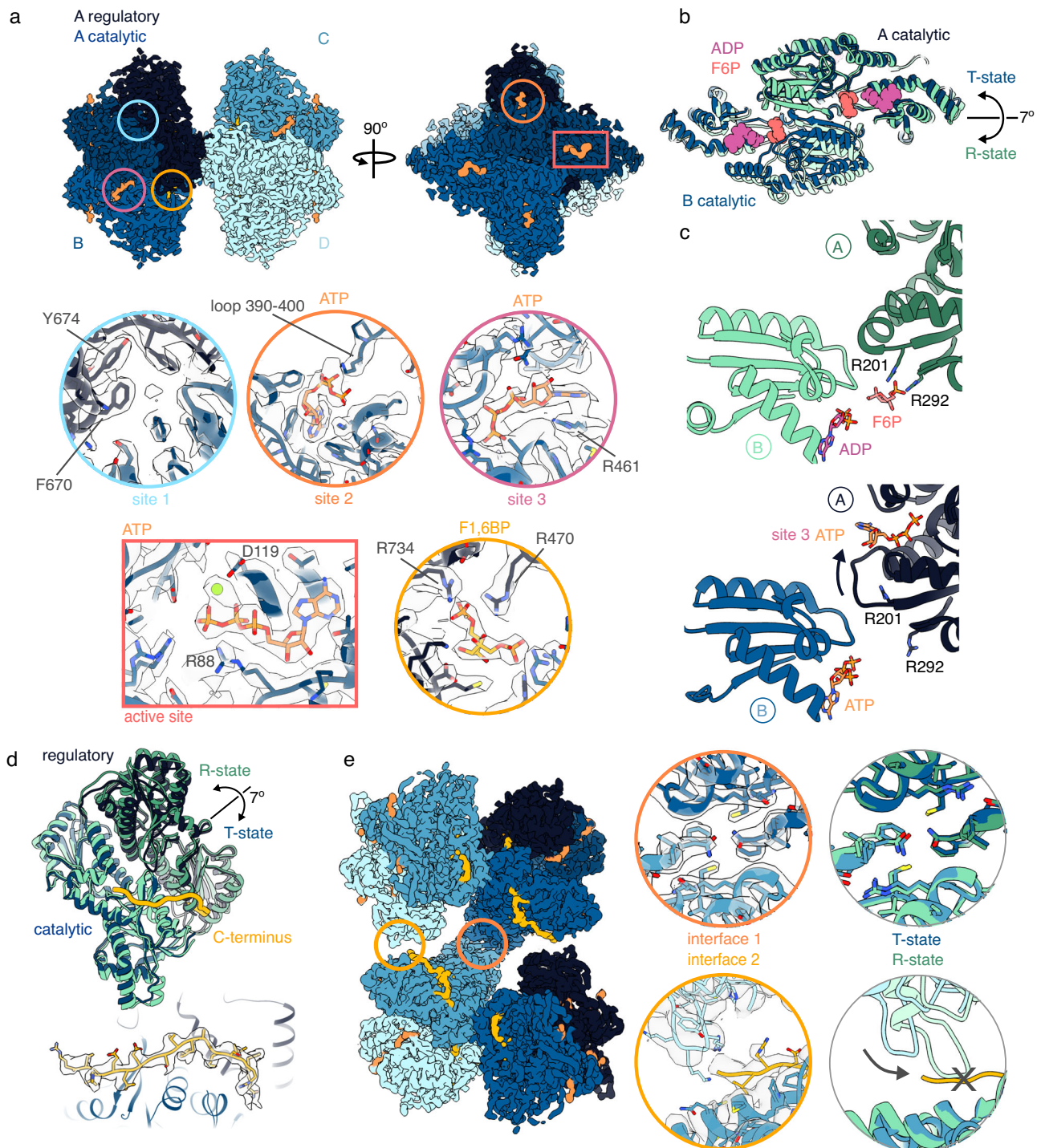


Fig. 2 | cryoEM structures of PFKL tetramers and filaments in the T-state.

a CryoEM structure of the consensus PFKL tetramer bound to ATP and fructose 1,6-bisphosphate (F1,6BP), colored by monomer. Monomer A is also colored by domain. Insets show the various ligand binding sites. **b** Comparison of the catalytic domain conformation of the ATP- and F1,6BP-bound structure (blue) with the R-state PFKL structure (green). Structures are aligned on the catalytic domain of subunit A. ADP and fructose 6-phosphate (F6P) from the R-state structure are shown in the active site. **c** Comparison of the F6P binding site in the R-state (green) and T-state (blue) structures. The binding site involves residues from the catalytic domains of two monomers (A and B). **d** Comparison of monomer conformations in

the R-state (green) and T-state (blue) structures. Structures are aligned on their catalytic domains (lighter shades). The C-terminus (yellow) bridges across the regulatory and catalytic domains in the T-state conformation. Lower panel shows the isolated density of the C-terminus from the T-state cryoEM map. **e** CryoEM structure of the T-state PFKL filament, colored by monomer. Circles show zoomed-in views of filament interfaces 1 and 2. Panels at right show comparisons to interfaces 1 and 2 in the R-state structure. Inward rotation of the catalytic domain at interface 2 in the R-state would produce a clash with the C-terminus at the position observed in the T-state structure.

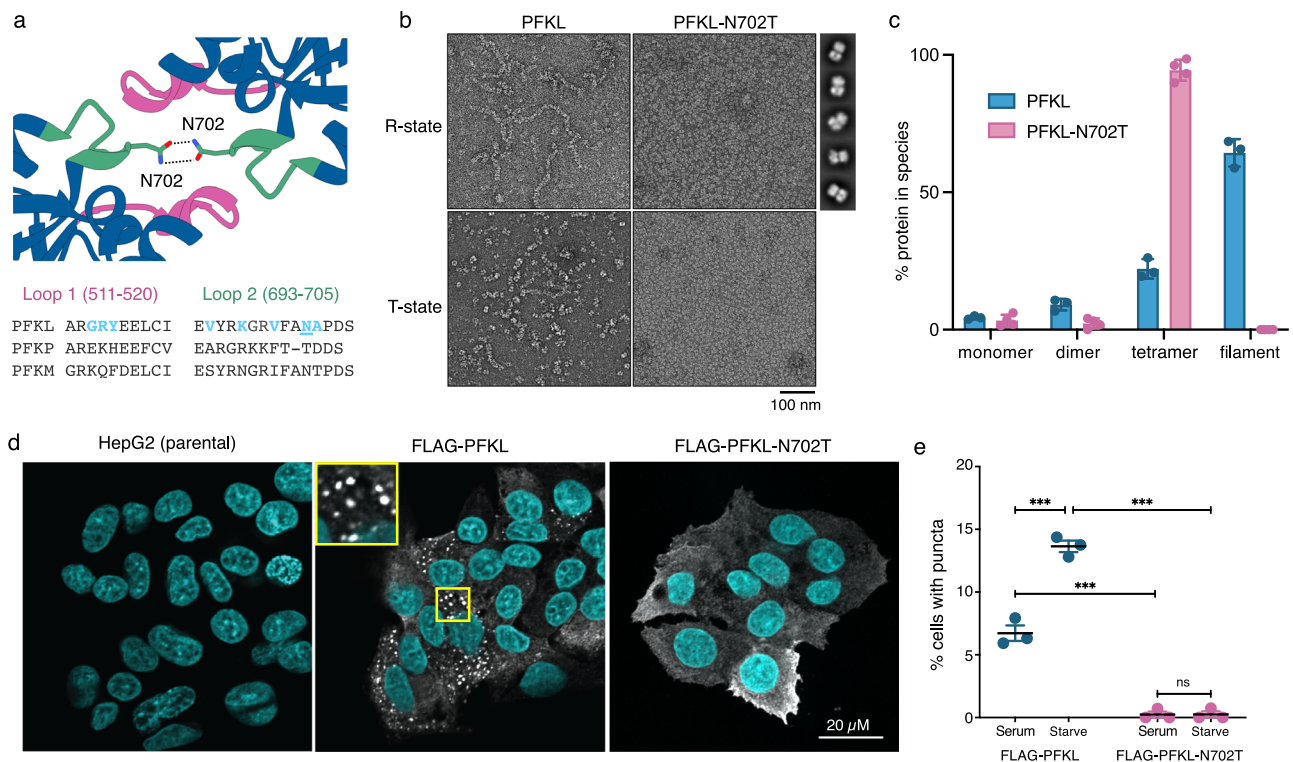


Fig. 3 | Filament interface 1 is essential for assembly of PFKL in vitro and in cells.

a Structure of PFKL filament interface 1 showing two loops forming the interface (top) and sequence alignment of interface 1 residues with other human isoforms (bottom). Poorly-conserved PFKL interface residues are highlighted in blue, with N702 underlined. **b** Negative stain EM showing that PFKL-N702T does not form filaments in either R-state or T-state ligand conditions. Panels at right show representative 2D class averages of PFKL-N702T tetramers in R-state conditions. Scale bar is 100 nm. **c** Quantification of assembly state of PFKL and PFKL-N702T by mass photometry. Relative abundance of oligomers was calculated as described in Methods. Data are presented as mean and standard deviation of $n = 3$ experiments for PFKL and $n = 4$ experiments for PFKL-N702T, with individual data points also

shown. **d** Immunofluorescent images of parental HepG2 cells and cells expressing wild type FLAG-PFKL or FLAG-PFKL-N702T labeled with anti-FLAG (white) and Hoechst 33342 (blue) under serum starved conditions. Puncta are only visible in wild type FLAG-PFKL cells. Inset shows a higher magnification view of the 10 μm by 10 μm area in the yellow box. Scale bar is 20 μm . **e** Quantification of the number of cells in continuous serum or in serum starved conditions containing PFKL punctae, as defined as cells with three or greater PFKL assemblies of at least 1 μm diameter. Data is representative of 3 independent passages of cells. Mean and SEM are shown, two-way ANOVA test (PFKL, serum vs starved $p = 0.0008$; N702T, serum vs starved $p = 0.9999$; Serum, PFKL vs N702T $p = 0.0001$; Starved, PFKL vs N702T $p = 0.0001$).

small rotation between the regulatory domains within catalytic dimers (Supplementary Fig. 3g), which produces a slight conformational change at the tetramer interface (Supplementary Fig. 3h).

T-state PFKL filaments have a similar overall architecture to R-state filaments, being composed of stacked tetramers (Fig. 2e). Interface 1 is the same in the T-state and R-state filament structures (Fig. 2e), while interdomain rotations in each protomer result in disruption of interface 2 interactions. In the T-state filament, loop 693–705 is rotated away from the binding groove on the adjoining tetramer, which is instead occupied by the C-terminus (Fig. 2d, e). Residues on loop 693–705 are in range to form contacts with the C-terminus in the T-state filament, though specific contacts were not well-resolved in this region. Inward rotation of loop 693–705 upon transition to the R-state conformation is sterically inhibited by a bound C-terminus in an adjoining T-state tetramer; in order for a tetramer within a filament to transition from the T-state to the R-state conformation, the C-termini of neighboring T-state tetramers must be displaced. Thus, competition at interface 2 between binding of a protomer's own C-terminus and loop 693–705 on a neighboring tetramer may provide a mechanism to allosterically couple T- to R-state transitions between tetramers within filaments. For both the R- and T-state filaments, the two adjoining protomers at interface 2 exhibit the same overall conformation despite being in different packing environments, with one protomer donating and the other receiving loop 693–705 (Ca RMSD 0.5Å and 0.2Å for the R- and T-state structures, respectively) (Supplementary Fig. 3i–k).

Cellular assembly of PFKL requires filament formation

Towards understanding the function of PFKL filaments, we generated a non-polymerizing PFKL mutant. PFKP does not assemble filaments¹⁸, and several residues at PFKL interface 1 differ between the isoforms (Fig. 3a). N702 at the core of PFKL interface 1 is substituted for threonine in PFKP, and we, therefore, expressed and purified the substitution mutant PFKL-N702T (Supplementary Fig. 4a). Negative stain EM confirmed that PFKL-N702T disrupted filament assembly in both R- and T-states, but did not disrupt tetramer formation (Fig. 3b). This result was confirmed by mass photometry: wild-type PFKL was predominantly filamentous, with 60% of protein in assemblies larger than tetramers, while PFKL-N702T was 90% tetrameric with no larger species observed (Fig. 3c, Supplementary Fig. 5a, b). Both samples also exhibited small populations of monomers and dimers (Fig. 3c). Enzyme assays revealed that filament formation had only a modest effect on enzyme activity and allosteric regulation: Compared with wild-type PFKL, PFKL-N702T exhibited a slight increase in maximal velocity, F6P affinity, and cooperativity, as well as a slight decrease in affinity for inhibitory ATP (Supplementary Fig. 4b).

PFKL assembles into micrometer-sized structures in the human hepatocellular carcinoma cell line HepG2²². We aimed to determine whether these higher-order structures observed in cells correspond to the PFKL filaments observed with purified protein. We, therefore, expressed N-terminally-tagged wild-type FLAG-PFKL or non-polymerizing FLAG-PFKL-N702T in HepG2 cells and imaged both by immunofluorescence (Fig. 3d, Supplementary Fig. 4c, d). In cells grown

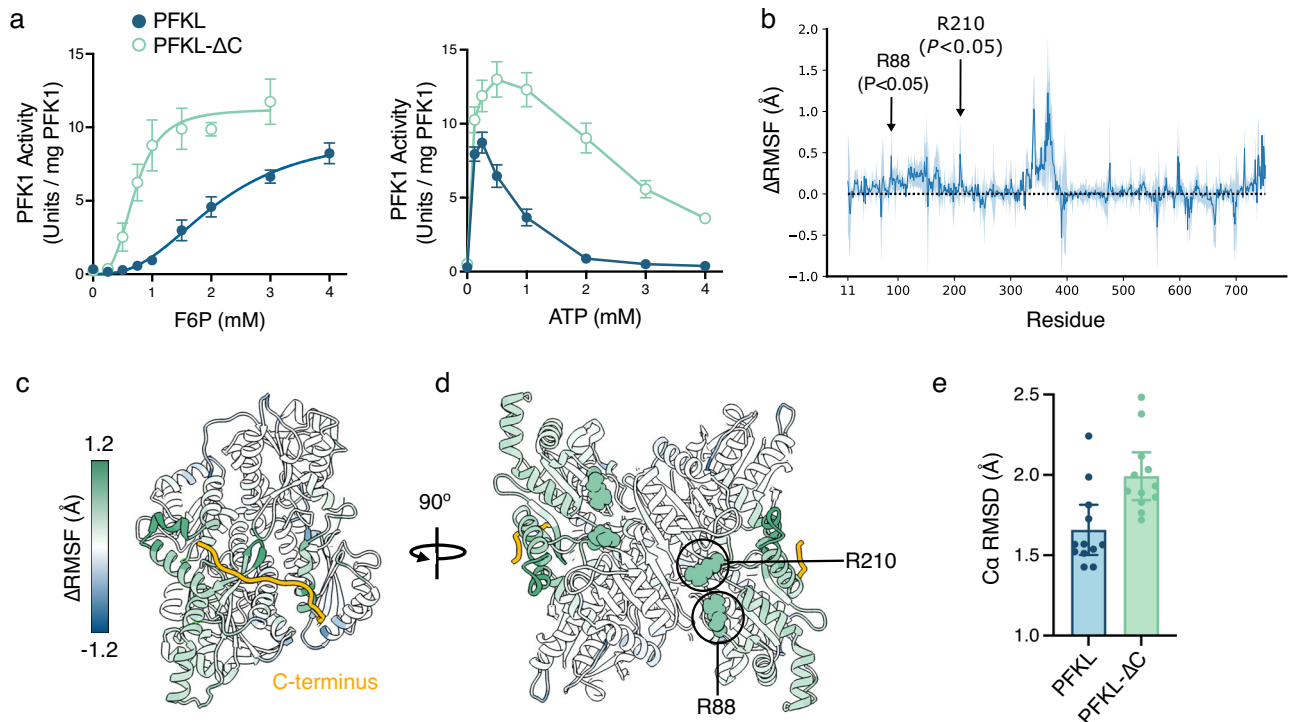


Fig. 4 | The C-terminal tail of PFKL stabilizes the T-state conformation.

a Enzyme activity assays to determine the affinity for F6P (left) and ATP (right) for wild type PFKL (blue) and PFKL-ΔC (green). Assay conditions are described in Table 1. F6P data are mean and SEM of $n = 7$ replicates for PFKL ($n = 6$ for 2 mM F6P, $n = 1$ for 0.25 mM F6P) and $n = 5$ replicates for PFKL-ΔC ($n = 2$ for 2 mM F6P). ATP data are mean and SEM of $n = 7$ replicates for PFKL and $n = 4$ replicates for PFKL-ΔC. **b** Difference in per-residue root-mean-square fluctuations (ΔRMSF) after C-terminal tail removal as observed in MD simulations. The light blue regions

correspond to the 95% confidence intervals. Arginine residues 88 and 210, involved in binding F6P in the R-state, are highlighted by arrows. **c, d** PFKL monomer with residues colored according to ΔRMSF values in **(b)**. Removal of the C-terminus produces elevated ΔRMSF values at the C-terminus binding site **(c)** and in the active site **(d)**. **e** Average Cα RMSD from the cryoEM structure of a T-state subunit during the last 200 ns of the MD simulations for PFKL and PFKL-ΔC. Data points represent values for a total of 12 protein subunits sampled in 3 simulation replicas. Error bars represent the 95% confidence intervals.

Table 1 | Kinetic parameters for wild type and mutant PFKL

	$K_{m,F6P} \pm SEM$ (mM)	Hill coefficient $\pm SEM$	$V_{max} \pm SEM$ (Units per mg PFK1)
PFKL ($n = 7$)	2.1 ± 0.3	2.6 ± 0.6	9.6 ± 1.4
PFKL-N702T ($n = 6$)	1.5 ± 0.1	3.9 ± 0.7	13.8 ± 0.8
PFKL-ΔC ($n = 5$)	0.8 ± 0.1	2.6 ± 0.5	10.6 ± 0.7

The kinetic parameters for PFKL were determined at pH 7.5 with 125 μM ATP. The parameters were generated by fitting data to the allosteric sigmoidal model. The number of experimental replicates is noted in parentheses.

in complete media containing 10% FBS, FLAG-PFKL had a diffuse cytoplasmic localization in a majority of cells. However, in 7% of cells FLAG-PFKL assembled into multiple structures greater than 1 μm in diameter (Fig. 3e, Supplementary Fig. 4d). We next asked if serum starvation altered the number of cells displaying puncta as withdrawal of insulin signaling decreases glucose uptake in HepG2 cells²³. In HepG2 cells that were incubated in media containing 0.1% FBS overnight, the percentage of cells containing FLAG-PFKL puncta doubled to 14% (Fig. 3d, e), suggesting that PFKL assembly is regulated by hormonal or growth factor signaling. In contrast, FLAG-PFKL-N702T was diffuse in both complete serum and serum starved conditions (Fig. 3d, e, Supplementary Fig. 4d), indicating that polymerization of PFKL into filaments is required for assembly of the micron-scale PFKL structures observed in cells.

The T-state of PFKL is stabilized by the C-terminal tail

The C-terminal tail is required for proper regulation of PFK1 in *Dicystostelium discoideum* and human PFKP^{8,24}, though the mechanism by which it imparts allosteric control of PFK1 has not been described. Notably, the C-terminal region of PFK1 shows substantial sequence

variation across species and also between the PFKL, PFKP, and PFKM isoforms (Supplementary Fig. 4e). To determine the role of the C-terminal tail in PFKL allosteric regulation, we purified a construct in which the C-terminal 28 amino acids were removed (PFKL-ΔC) and tested its activity and regulation. As shown for other human PFK1 isoforms⁸, removal of the C-terminal tail increased affinity for the sugar substrate F6P and relieved allosteric inhibition by ATP (Fig. 4a, Table 1). Negative stain EM and mass photometry indicated that truncation of the C-terminus had no major effect on tetramer or filament formation compared with the wild-type enzyme (Supplementary Fig. 4f, g, Supplementary Fig. 5c).

Given that the PFKL C-terminal tail was only resolved in the T-state cryoEM structure, we hypothesize that the C-terminal tail stabilizes PFKL in the less active T-state conformation and removal of these residues would promote transition to the R-state. To test this hypothesis, we performed molecular dynamics (MD) simulations and asked if removal of the tail altered the conformation of the enzyme. We ran three independent 400 ns MD simulations with the C-terminal tail included (residues 753–780) using the CHARMM36m protein force field²⁵, and we repeated the same computational protocol for the

structure lacking the C-terminal tail. The simulations showed that removal of the C-terminus destabilizes the T-state structure, as quantified by the difference in per-residue root-mean-square fluctuations (Δ RMSF) (Fig. 4b–d). The structural changes mainly concerned the region of residues -330–380 and notably residue 715 on the solvent-exposed side of the subunit. These residues correspond to the region of PFKL where the C-terminal tail binds. Additionally, some of the residues surrounding the catalytic site show a change in structure, specifically residues involved in binding F6P (R88 and R210), suggesting that conformational changes caused by removal of the C-terminal tail propagate to the active site. The overall conformation of PFKL subunits transitions away from the T-state upon the C-terminal tail removal, as measured by the average C α RMSD from the cryoEM structure of the T-state (Fig. 4e). We note, however, that the current MD simulations do not show a statistically significant decrease in the C α RMSD from the cryoEM structure of the R-state (Supplementary Fig. 6a). In fact, our simulations indicate an overall destabilizing effect of the C-terminal tail removal on the time scale of hundreds of nanoseconds (see Supplementary Fig. 9 for the time-course analysis of the MD results, showing consistent trends among the simulation replicas). However, the time scale of the complete transition between the T- and R-states, which may also require changes in allosteric site occupancies, likely exceeds that of the simulations. Therefore, a combination of enhanced sampling simulation methods may be necessary to sample the complete transition and evaluate the relative populations of the T- and R-states.

When the C-terminal tail conformation is transferred from the T-state to the R-state, the region of the C-terminus resolved in the T-state structure remains bound to the protein surface on the time-scale of the MD trajectories (3×400 ns). However, as a consequence of the altered domain angle in the R-state, we observe a strong decrease in the interactions between this region and the region formed by residues 680–740 of the regulatory domain (Supplementary Fig. 6b, c), including the loss of the electrostatic interaction between residues K715 and E767. These interactions, which are lost in the R-state and upon C-terminal tail truncation, likely contribute to T-state stabilization by helping to maintain the domain angle characteristic of the T-state.

To further describe the impact of the C-terminal tail on the T-state, we analyzed the dynamic coupling of the C-terminal tail residues with the active site and the allosteric sites 1 and 3, which change their occupancies between the T- and R- structures. Using ensemble correlation network analysis²⁶ (see Methods), a method relying on the analysis of nanosecond-scale motions of protein residues, we constructed a network of inter-residue correlations based on our MD trajectories of the T-state. For each residue of the C-terminal tail, we then identified the optimal and suboptimal network paths to residues from the sites of interest, as shown in Supplementary Fig. 7. The path lengths between two source and sink residues express the coupling strength, with shorter pathways corresponding to a tighter dynamic coupling between the two residues.

We found that the coupling strength varies along the sequence of the C-terminal tail. The tightest coupling to the active site and the allosteric sites 1 and 3 is displayed by residues near the beginning of the C-terminal tail domain (residues 753–756) and residues in the region -765–771, where the C-terminal tail is bound to the adjacent β -strand 342–347 (Supplementary Fig. 7a). The C-terminal tail residues 765–771 exhibit a tight coupling to the active site residue R210 via portions of the β -strand 342–347, α -helix 348–364 and the loop 163–176 (see Supplementary Fig. 7b). These secondary structure elements are also crossed by paths leading to the active site residue R201, involved in the T-R transition (Supplementary Fig. 7c in SI). Paths of comparable length couple residues 765–771 to the active site residue R201 from the neighboring subunit (Supplementary Fig. 7c). Routes connecting the C-terminal residues 765–771 to the allosteric site 1

(residue K677) cross the interface between the β -hairpin 334–347 of the catalytic domain and the β -hairpin 707–721 of the regulatory domain (Supplementary Fig. 7d). This suggests an important role of this interface in mediating the allosteric coupling of the C-terminal tail and site 1. Further, the C-terminal tail residues are coupled more strongly (i.e., via shorter paths) to the residue T194 from the allosteric site 3 of the neighboring subunit than to this residue in the same subunit (Supplementary Fig. 7a and Supplementary Fig. 7e). Residue T194 as well as several other residues from the helix that undergoes local unfolding upon ATP binding at site 3 exhibit the highest density of dynamic connections, as measured by node centrality (Supplementary Fig. 8). The high density of dynamic connections underlines the importance of site 3 for the allosteric regulation of PFKL.

Discussion

The regulation of PFK1 is a textbook example of allostery, with substrate, activators, and inhibitors competing to shift the enzyme between the active R-state and inactive T-state conformations. However, much of the structural insight into PFK1 regulation has been limited to the bacterial enzyme, with all existing structures of vertebrate PFK1 exhibiting the R-state conformation^{7,8}. The R-state PFKL structure presented here resembles existing R-state PFK1 structures indicating—perhaps unsurprisingly—that a particular, conserved conformation is necessary for catalytic activity. By contrast, T-state PFKL differs from existing T-state structures, exhibiting a different overall conformation, an additional allosteric ATP-binding site, as well as additional regulation through binding of the C-terminal tail. Previous studies have shown that insulin induces phosphorylation of the PFKL C-terminus, increasing PFKL activity and flow through glycolysis²⁷. Based on the structures presented here, it seems plausible that phosphorylation could displace the PFKL C-terminus, thus favoring the R-state conformation and increasing enzymatic activity. There is substantial sequence variation in the C-terminal tails between human PFKL, PFKP, and PFKM, perhaps providing an additional mechanism for differential regulation of the isoforms. Given the large number of ligands known to regulate PFK1 activity, additional structures in different ligand states are certainly warranted and may lead to identification of additional PFK1 conformations.

PFKL filaments are somewhat unique in comparison to filaments of other metabolic enzymes. As with many other enzyme filaments, PFKL filaments are polymers of a subunit with dihedral symmetry^{28–30}—filaments of this sort may be the simplest to evolve, with a single, symmetric interface allowing for propagation of an unbounded polymer^{31,32}. For most enzyme filaments, the helical axis is coincident with a symmetry axis within the core, dihedral protomer, producing filaments with a linear architecture. With PFKL filaments, however, incoming tetramers can associate at one of two different positions on a filament end, resulting in both straight and bent architectures¹⁸. Notably, these variable architectures emerge despite the fact that each individual filament interface is the same.

Enzyme filaments variously function to increase or decrease enzyme activity^{33–37}, increase cooperativity in regulation³³, facilitate substrate channeling^{38,39}, and tune affinity for regulatory ligands^{40–43}. PFKL filaments differ in having no major direct effect on enzyme activity or regulation, and their function may therefore only be apparent in the context of the cell. Indeed, under conditions of energy stress, PFK1 assembles with other glycolytic enzymes into cellular foci which appear to both increase the rate of glycolysis and localize energy production to particular subcellular sites^{22,44,45}. In neurons, for example, PFK1 assemblies appear at synapses, where there is an increased demand for ATP production⁴⁴. PFKL assemblies have also been observed near the plasma membrane, where they could function to increase local ATP concentrations to support endocytosis, protrusion, and active transport¹⁸. These assemblies may increase the rate of glycolysis by enabling more efficient transfer of substrates between members of the glycolytic

pathway. The fact that PFKL can form filaments with a range of bent and straight architectures suggests that long-range order of PFKL oligomers may be less important than aggregation of many copies of the enzyme in one location in the cell. This would be consistent with a scaffolding role of PFKL in assembly of condensates containing multiple glycolytic enzymes. The PFKL-N702 non-polymerizing mutant provides a tool to address the functional role of PFKL assembly in cells and to determine if the higher-order assembly of other glycolytic enzymes depends on PFKL polymerization.

In summary, the present study provides a detailed structural understanding of the allosteric regulation of eukaryotic PFKL. These structural insights will aid in the development of small molecule compounds specifically designed to target PFKL. Pharmacologically targeting glycolytic enzymes is a proposed therapeutic approach for the treatment of diseases in which glucose metabolism is dysregulated. For example, proliferative cancer cells have an increased reliance on glycolysis to generate energy and biosynthetic precursors to support their rapid proliferation, which may make them susceptible to inhibition of glycolytic flux. However, there are currently no specific, high-affinity PFKL inhibitors available; generating small molecules that can stabilize the T-state, possibly by stabilizing the C-terminal tail-bound conformation, is an area of future research.

Methods

Expression, purification, and activity of recombinant PFKL

Wild type and mutant recombinant human (NP_002617) with an amino terminal His-tag was expressed in sf9 cells using the Bac-to-Bac Expression system (Invitrogen)¹⁸. 2×10^8 sf9 cells were used to express PFKL at an estimated multiplicity of infection of 2 viral particles per cell for 48 h. Cells were resuspended in lysis buffer (20 mM TRIS hydrochloride, pH 7.5; 80 mM potassium phosphate; 1 mM 2-mercaptoethanol; 10% glycerol; 10 mM imidazole, and EDTA-free Protease Inhibitor Cocktail (Abcam) and lysed with 20 passes of a Dounce homogenizer. Lysates were cleared by centrifugation and the supernatants were incubated with 5 ml HisPur cobalt resin (ThermoFisher Scientific). The resin was washed with 5 bed volumes lysis buffer, 10 bed volumes high salt lysis buffer containing 1 M NaCl, and 5 bed volumes lysis buffer. PFKL was eluted in lysis buffer supplemented with 100 mM imidazole. Fractions containing protein were pooled, and the buffer was exchanged for freezing buffer (20 mM 4-(2-hydroxyethyl)-1-piperazineethanesulfonic acid, pH 7.5; 1 mM DTT; 500 μ M ammonium sulfate; 5% glycerol; 1 mM ATP, and 100 μ M EDTA) using a HiPrep 26/10 desalting column (GE Healthcare Life Sciences). Proteins were concentrated using an Amicon Ultracel-30K Centrifugal Filter Unit (MilliporeSigma) and their concentrations determined using a Bradford Protein Assay (ThermoFisher Scientific). Small aliquots of PFKL were snap frozen in liquid nitrogen and stored at -80°C . PFKL-Asn702Thr point mutant was generated by using a commercially available site-directed mutagenesis kit (QuikChange Lightning; Agilent Technologies). DNA primers were designed using an online primer design tool (Agilent Technologies) and were purchased from Integrated DNA Technologies, Inc. The presence of the mutations and the integrity of the constructs were verified by Sanger sequencing (WVU Genomics Core). PFKL activity was determined using an auxiliary enzyme assay to monitor the production of fructose 1,6-phosphate adapted for use in a 96-well format, as previously described^{7,18,46}. The absorbance at 340 nm was measured using a Varioskan LUX Multimode microplate reader (ThermoFisher). Kinetic parameters were generated by nonlinear regression analysis using Prism (GraphPad Software) and are the mean of a minimum of three measurements from two independent preparations of protein. One unit of activity was defined as the amount of enzyme that catalyzed the formation of 1 μ mol of fructose 1,6-bisphosphate per minute at 25°C . F6P affinity was determined at pH 7.5 with 0.125 mM ATP. ATP inhibition was determined at pH 7.5 with 4 mM F6P.

Negative stain electron microscopy

Negative stain samples were prepared by diluting freshly thawed protein to 1 μ M in 50 mM HEPES pH 7.5, 20 mM $(\text{NH}_4)_2\text{SO}_4$, 10 mM MgCl_2 , 2 mM ADP, 2 mM F6P to promote the R-state conformation or in 50 mM HEPES pH 7.5, 20 mM $(\text{NH}_4)_2\text{SO}_4$, 10 mM MgCl_2 , 4 mM ATP, 0.5 mM F1,6BP to promote the T-state conformation. The protein was applied to glow-discharged carbon-coated grids, washed three times with water, and stained with 2% (w/v) uranyl formate. Grids were imaged using a 120 kV FEI Spirit microscope with a $4k \times 4k$ Gatan Ultrascan CCD camera. Micrographs used to generate 2D negative stain averages of PFKL N702T were acquired on a sample containing 250 nM PFKL N702T in 50 mM HEPES pH 7.5, 20 mM $(\text{NH}_4)_2\text{SO}_4$, 10 mM MgCl_2 , 2 mM ADP, 2 mM F6P, prepared as described above. Automated collection of negative stain micrographs was performed using the Legikon software⁴⁷. 240 micrographs were collected with defocus values ranging from -2 to $-1 \mu\text{m}$ and an average electron dose of ~ 50 electrons/ \AA^2 . CTF parameters were estimated with CTFIND4⁴⁸. Particles were selected using Blob Picker, then extracted and subjected to three rounds of reference-free 2D classification in cryoSPARC⁴⁹.

CryoEM sample preparation, data collection, and data processing

CryoEM samples were prepared by applying protein to CFLAT 2/2 holey carbon grids (Protochips) and blotting away liquid four times successively before plunging into liquid ethane using a VitroBot (ThermoFisher). Samples used to determine R-state structures contained 9 μ M PFKL, 2 mM F6P, and 1 mM ATP in storage buffer (20 mM HEPES pH 7.5, 1 mM DTT, 500 μ M ammonium sulfate, 5% glycerol, 100 μ M EDTA). Samples used to determine T-state structures contained 2 mM ATP, 10 mM MgCl_2 , and 500 μ M F1,6BP in storage buffer. For R-state PFKL structures, movies were collected on a Titan Krios (ThermoFisher) equipped with a K3 Direct Detect Camera (Gatan Inc.) operating in superresolution mode with a pixel size of $0.4215 \text{ \AA}/\text{pixel}$, 75 frames, and a total dose of 63 electrons/ \AA^2 . For T-state PFKL structures, movies were collected on a Titan Krios equipped with a K2 Direct Detect Camera (Gatan Inc.) operating in superresolution mode with a pixel size of $0.525 \text{ \AA}/\text{pixel}$, 50 frames, and a total dose of 90 electrons/ \AA^2 . A subset of the data for the T-state sample was collected at 30° tilt. Data collection was automated with Legikon software⁴⁷. CryoEM data was processed using cryoSPARC⁴⁹, and processing workflows are summarized in Supplementary Figs. 1, 2. Super-resolution movies were motion corrected, dose-weighted, and binned 2X using patch motion correction. CTF parameters were estimated using patch CTF. Particles were picked using the blob picker and subjected to multiple rounds of 2D classification. Initial 3D refinements were performed with combined particles representing both filaments and free tetramers, using a tetramer starting reference. Tetramers and filaments were then separated by 3D classification (without alignment) and refined independently with D2 and C2 symmetry, respectively. Additional rounds of 3D classification were performed to remove poor quality and damaged particles (Supplementary Figs. 1, 2). Masked, local refinement of filament interface 1 was performed using a mask encompassing the two dimers associated across interface 1. Per-particle defocus, beamtilt, and spherical aberration were also refined for all structures. Density modification was performed using Resolve-Cryoem in Phenix⁵⁰. Atomic models were built using ISOLDE⁵¹ and real-space refinement in Phenix. Structures were visualized with UCSF Chimera⁵². Cryo-EM data collection, refinement, and validation statistics are summarized in Supplementary Table 1.

Mass photometry experiments and analysis

Mass photometry experiments were performed using the TwoMP system by Refeyn⁵³. PFKL filaments were assembled by diluting freshly thawed PFKL to 2.5 μ M in cold dilution buffer (50 mM HEPES pH 7.5, 100 mM KCl). The 2.5 μ M PFKL sample was diluted to 250 nM in cold

polymerization buffer (50 mM HEPES pH 7.5, 100 mM KCl, 20 mM $(\text{NH}_4)_2\text{SO}_4$, 10 mM MgCl_2 , 2 mM ADP, 2 mM F6P). The samples were incubated on ice for 2 min before they were diluted tenfold into a droplet of room temperature MP buffer (50 mM HEPES, pH 7.5, 50 mM KCl). As PFKL-N702T was predominantly tetrameric with no protein sequestered into larger-order oligomers, it was diluted 20-fold for a final concentration of 12.5 nM to obtain a measurable number of binding events. Movies were recorded immediately following dilution. Binding events were measured at a rate of 600 frames/min for one minute. Mass calibrations were performed with 5–10 nM each of beta-amylase, apoferritin, and glutamate dehydrogenase. Movies were collected with AcquireMP v2.3 and data was analyzed using DiscoverMP v2.3. To compare the relative populations of PFKL species in each movie, the counts per species was determined by the area under the curve of a Gaussian fit to the histogram of mass species using the DiscoverMP v2.3 software (Refeyn Ltd). This number was normalized to account for the number of PFKL monomers per species and converted to a percent of the total counts per species per movie. These percentages were averaged across replicates and compared among PFKL wild-type and mutants. Error bars represent the standard deviation. At least three replicates were performed for each sample. Representative histograms of PFKL and mutants are shown in Supplementary Fig. 5.

Generation and imaging of HepG2 cells

HepG2 cells were purchased from ATCC (HB-8065), were authenticated by ATCC using short tandem repeat (STR) testing, and were verified to be mycoplasma-free. Cells were grown in high glucose DMEM (ThermoFisher Scientific) supplemented with 10% Heat Inactivated Fetal Bovine Serum (FBS; ThermoFisher Scientific) and 1% penicillin/streptomycin (ThermoFisher Scientific) in a 37 °C tissue culture incubator with 5% CO_2 . FLAG-PFKL and FLAG-PFKL-N702T were cloned into a pLenti6.3 vector (ThermoFisher Scientific). The presence of the mutations and the integrity of the constructs were verified by Sanger sequencing. HepG2 cells expressing FLAG-PFKL were generated as previously described⁵⁴. Lentivirus was generated using HEK293^{FT} cells (ATCC) and ViralPower lentiviral packaging mix (ThermoFisher Scientific), according to the manufacturer instructions. Blasticidin-resistant cells were pooled and used in experiments. The expression of exogenous FLAG-PFKL was verified by western blot (WB) analysis using primary antibodies generated against FLAG and PFKL, while GAPDH was used as a loading control.

For immunofluorescent (IF) analysis, parental HepG2 cells or cells expressing FLAG-PFKL or FLAG-PFKL-N702T were plated on 1.5 mm glass coverslips and incubated overnight at 37 °C. Cells were washed with PBS and the media was replaced with media containing either 0.1% or 10% FBS. The next day, cells were rinsed in PBS, fixed in 4% paraformaldehyde, and permeabilized in 0.1% Triton X-100. Coverslips were blocked in blocking buffer (3% BSA, 1% non-immune goat serum, 1% cold water fish gelatin) at room temperature for 30 min. Primary antibodies to FLAG were used at a 1:1000 in blocking buffer and incubated at 37 °C for 2 h. Coverslips were incubated with secondary goat anti-mouse antibodies labeled with Alexa Fluor-488 and Hoechst-33342 (ThermoFisher Scientific; Ref:H3570; Lot: 1932770; 1:10,000 dilution) for 30 min at 37 °C. Coverslips were mounted on glass slides with ProlongTM Gold antifade reagent (ThermoFisher Scientific), allowed to cure overnight, and sealed with nail polish. Coverslips were imaged using a Nikon TI2-E Inverted Microscope with a CSU-W1 Confocal Scanner spinning disk with a 60× oil immersion objective. Image processing was performed in NIS Elements and ImageJ. To quantify the ability of wild type and N702T FLAG-PFKL to form punctae in cells, we counted the percentage of cells with greater than three FLAG assemblies of at least 1 μm in diameter. Between 100 and 150 cells were counted in each experimental group for three independent passages of cells. Two-way

ANOVA was performed to determine statistical significance using GraphPad Prism software.

The antibodies used were: Monoclonal anti-FLAG M2, Sigma Aldrich, Ref: F1804, Lot: 00002788731, IF: 1:500 dilution, WB 1:1000 dilution; Rabbit monoclonal anti-PFKL antibody, Abcam, Ref: ab181064, Lot: GR164226-1, WB: 1:1000 dilution; Rabbit monoclonal GAPDH D16H11, Cell Signaling Technologies, Ref: 5174, Lot: 8, WB: 1:2000 dilution; Alexa Fluor-488 goat anti-mouse IgG (H+L), Invitrogen Ref: A11001, Lot: 2610355, IF: 1:500 dilution; Donkey anti-mouse IgG Secondary Antibody, HRP, Jackson Immuno Research, Ref: 715-035-150, Lot: 150088, WB: 1:20,000 dilution; Donkey anti-rabbit IgG Secondary Antibody, HRP, Jackson Immuno Research, Ref: 711-035-152, Lot: 156087 WB: 1:10,000 dilution.

MD simulations

The cryoEM structure of the PFKL tetramer in the T-state including the ATP and F1,6BP ligands was used as the starting point for all-atom MD simulations. For simulations involving the full-length C-terminal tail, the initial positions of the nine C-terminal residues, which were not resolved in the cryo-EM structure, were modeled using PyMOL software version 2.5.4⁵⁵. For simulations of the PFKL-ΔC construct, the structure of each subunit was truncated after residue 752. The first 10 N-terminal residues, which were missing from the experimental structure, were not included in the simulations. The protonation states of histidine residues were adopted from the experimental structure. In addition, MD simulations were performed starting from the cryoEM structure of the R-state tetramer including the ADP, F6P, and F1,6BP ligands and with the full-length C-terminal tail transferred from an equilibrated geometry of the T-state.

The GROMACS pdb2gmx tool⁵⁶ (version 2022.5) was used for protein topology preparation, and the CHARMM36m²⁵ force field, a structure-balanced all-atom force field suitable for the description of both folded and intrinsically disordered proteins, was employed to describe the protein. Existing CHARMM parameters for ATP and ADP were obtained from the CHARMM-GUI webserver^{57,58}, and the same web server was employed to parameterize the F1,6BP and F6P molecules using the CHARMM General Force Field (CGenFF)⁵⁹. Water molecules were described with the TIP3P model⁶⁰, and K^+ and Cl^- ions were modeled using the default ion parameters associated with the CHARMM36m force field. To allow for a longer time step in production simulations, the hydrogen mass repartitioning scheme⁶¹, transferring the mass of 3 Da to a hydrogen atom from the nearest heavy atom, was applied to protein and ligand hydrogen atoms.

The PFKL tetramer was placed in a rhombic dodecahedral simulation box with the nearest-image distance of 20.1 nm and 18.7 nm for the T-state system with and without the C-terminal tail, respectively, and 18.9 nm for the R-state system. The protein was solvated in a 150 mM KCl aqueous solution, including additional K^+ ions to neutralize the net negative charge of the ligand-bound protein. In total, the system contained -569,000, -451,000, and -470,000 atoms, respectively. The system setup is summarized in Supplementary Table 3.

All-atom MD simulations were performed in the GROMACS 2022.5 software⁵⁶. Short-range non-bonded interactions were treated with a 1.2 nm cutoff, and van der Waals forces were smoothly switched to zero between 1.0 and 1.2 nm. Long-range electrostatic interactions were computed using the particle mesh Ewald method⁶². The leap-frog algorithm⁶³ was used to numerically integrate Newton's equations of motion. The LINCS algorithm⁶⁴ was employed to constrain the lengths of all hydrogen-involving protein bonds, with the highest order in the expansion of the constraint coupling matrix being increased from 4 to 6 in production simulations to achieve better accuracy with the longer time step used. The SETTLE algorithm⁶⁵ was utilized to keep water molecules rigid.

To gently relax the protein structure in the simulation box, the system was subjected to an energy-minimization and equilibration

protocol. First, an energy minimization was performed to decrease the maximum force below $1000 \text{ kJ mol}^{-1} \text{ nm}^{-1}$, while harmonic restraints were applied to all heavy atoms of the protein and those of the ligands (with a force constant $k_{\text{BB}} = 1000 \text{ kJ mol}^{-1} \text{ nm}^{-2}$ assigned to the protein backbone atoms as well as the ligand atoms and a force constant $k_{\text{SC}} = 500 \text{ kJ mol}^{-1} \text{ nm}^{-2}$ applied to the side-chain atoms). This energy minimization was followed by a six-step relaxation protocol during which the harmonic position restraints were gradually decreased. The first two steps of the equilibration protocol were performed in the NVT ensemble and were followed by four NPT simulations (see Supplementary Table 2 for more details).

The production simulations were performed with an extended time step of 4 fs, enabled by the use of the hydrogen mass repartitioning approach⁶¹. The length of each production trajectory was 400 ns. For each system, a set of three independent production trajectories was obtained, each started after independent minimization and equilibration of the initial structure. The trajectory frames were saved every 200 ps.

In equilibration simulations, the temperature of the system was maintained at 300 K by the Berendsen thermostat⁶⁶ with a time constant of 1 ps, and where applicable, the pressure was kept constant at 1.01 bar by the Berendsen barostat with the same time parameter. In production simulations, performed at the same temperature and pressure as the equilibration, the velocity rescaling thermostat with a stochastic term⁶⁷ was used with a time constant of 0.1 ps, and the Parrinello-Rahman barostat⁶⁸ was employed with a time constant of 1 ps. In all cases, the thermostats were coupled separately to the protein and to the rest of the system.

The per-residue RMSF were calculated separately for each subunit and over each production trajectory using the GROMACS RMSF tool⁶⁶ by considering the positions of all the atoms forming each residue. To describe the effect of the C-terminal tail removal, the differences in the per-residue means of these values were calculated between the PFKL and PFKL- Δ C systems. The *P*-values as well as the 95% confidence intervals of these differences were determined by performing a two-sided unpaired *t*-test using the Pingouin package⁴⁸ (version 0.5.3).

The root-mean-square deviation of C α atoms (C α RMSD) relative to the cryoEM structures of the T-state and R-state was computed using the MDAnalysis package⁶⁹ (version 2.7.0) for residues 20–752 in each subunit after aligning the subunit with a cryoEM subunit. The C α atoms of residues 20–752 were used for the alignment. For each subunit, the average C α RMSD over the second half of the production trajectory was calculated, and the mean of these values obtained for all the subunits and independent production trajectories was reported together with 95% confidence intervals estimated using Student's *t*-distribution.

Correlation network analysis

To describe the network of correlated motions in the T-state of PFKL, we conducted ensemble correlation network analysis²⁶ (eCNA) implemented in the Bio3D package⁷⁰ (version 2.4.4). In the eCNA approach, significant dynamic cross-correlation values (c_{ij}) between residues are identified across multiple simulation replicas to build a consensus network graph with edge weights determined from the c_{ij} values²⁶. Specifically, cross-correlations between C α atoms were calculated from the MD trajectories for each subunit after mass-weighted superposition of the dimer formed by the subunit and its neighboring subunit across the catalytic interface. The initial 50 ns of each trajectory were excluded from the analysis. Network edges were added for (1) residue pairs with $|c_{ij}| \geq 0.5$ for all subunits and all trajectories and (2) residues satisfying $|c_{ij}| \geq 0.5$ for at least one subunit and trajectory and with a C α -C α distance $\leq 10 \text{ \AA}$ for at least 75% of total simulation frames. Node centralities, expressing the density of connections per node²⁶, were computed using the Bio3D package. Network path analysis was performed using the Bio3D package to identify the optimal

and suboptimal network paths connecting selected pairs of source and sink residues. Path length distributions, indicating the strength of the dynamic coupling between the source and sink residues, were then evaluated. A total of 500 paths were generated for each residue pair. Normalized node degeneracy, defined as the fraction of the number of paths crossing each residue, was computed. The resulting paths were visualized using the VMD software⁷¹ (version 1.9.3).

Reporting summary

Further information on research design is available in the Nature Portfolio Reporting Summary linked to this article.

Data availability

Cryo-EM structures and atomic models have been deposited in the Electron Microscopy Data Bank (EMDB) and Protein Data Bank (PDB), respectively, with the following accession codes: EMD-43747, PDB: 8W2G (R-state PFKL tetramer); EMD-43749, PDB: 8W2I (R-state PFKL filament); EMD-43748, PDB: 8W2H (T-state PFKL tetramer); EMD-43750, PDB: 8W2J (T-state PFKL filament). MD simulation input files and final geometries, as well as node degeneracies from network path analysis, are available on Zenodo (<https://doi.org/10.5281/zenodo.12168317>). The reference structure used in this work is 4XYJ. Source Data are provided as a Source Data file. Source data are provided with this paper.

References

- Evans, P. R., Farrants, G. W. & Lawrence, M. C. Crystallographic structure of allosterically inhibited phosphofructokinase at 7 Å resolution. *J. Mol. Biol.* **191**, 713–720 (1986).
- Schirmer, T. & Evans, P. R. Structural basis of the allosteric behaviour of phosphofructokinase. *Nature* **343**, 140–145 (1990).
- Evans, P. R., Farrants, G. W. & Hudson, P. J. Phosphofructokinase: structure and control. *Philos. Trans. R. Soc. Lond. B Biol. Sci.* **293**, 53–62 (1981).
- Poorman, R. A., Randolph, A., Kemp, R. G. & Heinrikson, R. L. Evolution of phosphofructokinase—gene duplication and creation of new effector sites. *Nature* **309**, 467–469 (1984).
- Kemp, R. G. & Gunasekera, D. Evolution of the allosteric ligand sites of mammalian phosphofructo-1-kinase. *Biochemistry* **41**, 9426–9430 (2002).
- Banaszak, K. et al. The crystal structures of eukaryotic phosphofructokinases from baker's yeast and rabbit skeletal muscle. *J. Mol. Biol.* **407**, 284–297 (2011).
- Webb, B. A. et al. Structures of human phosphofructokinase-1 and atomic basis of cancer-associated mutations. *Nature* **523**, 111–114 (2015).
- Kloos, M., Brüser, A., Kirchberger, J., Schöneberg, T. & Sträter, N. Crystal structure of human platelet phosphofructokinase-1 locked in an activated conformation. *Biochem. J.* **469**, 421–432 (2015).
- Zancan, P., Marinho-Carvalho, M. M., Faber-Barata, J., Dellias, J. M. M. & Sola-Penna, M. ATP and fructose-2,6-bisphosphate regulate skeletal muscle 6-phosphofructo-1-kinase by altering its quaternary structure. *IUBMB Life* **60**, 526–533 (2008).
- Hesterberg, L. K. & Lee, J. C. Self-association of rabbit muscle phosphofructokinase: effects of ligands. *Biochemistry* **21**, 216–222 (1982).
- Costa Leite, T., Da Silva, D., Guimarães Coelho, R., Zancan, P. & Sola-Penna, M. Lactate favours the dissociation of skeletal muscle 6-phosphofructo-1-kinase tetramers down-regulating the enzyme and muscle glycolysis. *Biochem. J.* **408**, 123–130 (2007).
- Hicks, K. G. et al. Protein-metabolite interactomics of carbohydrate metabolism reveal regulation of lactate dehydrogenase. *Science* **379**, 996–1003 (2023).
- Yi, W. et al. Phosphofructokinase 1 glycosylation regulates cell growth and metabolism. *Science* **337**, 975–980 (2012).

14. Zhao, S. et al. Regulation of cellular metabolism by protein lysine acetylation. *Science* **327**, 1000–1004 (2010).
15. Mahrenholz, A. M., Lan, L. & Mansour, T. E. Phosphorylation of heart phosphofructokinase by Ca²⁺ calmodulin protein kinase. *Biochem. Biophys. Res. Commun.* **174**, 1255–1259 (1991).
16. Lee, J.-H. et al. Stabilization of phosphofructokinase 1 platelet isoform by AKT promotes tumorigenesis. *Nat. Commun.* **8**, 949 (2017).
17. Fernandes, P. M., Kinkead, J., McNae, I., Michels, P. A. M. & Walkinshaw, M. D. Biochemical and transcript level differences between the three human phosphofructokinases show optimisation of each isoform for specific metabolic niches. *Biochem. J.* **477**, 4425–4441 (2020).
18. Webb, B. A., Dosey, A. M., Wittmann, T., Kollman, J. M. & Barber, D. L. The glycolytic enzyme phosphofructokinase-1 assembles into filaments. *J. Cell Biol.* **216**, 2305–2313 (2017).
19. Amara, N. et al. Selective activation of PFKL suppresses the phagocytic oxidative burst. *Cell* **184**, 4480–4494.e15 (2021).
20. Rizzo, S. C. & Eckel, R. E. Control of glycolysis in human erythrocytes by inorganic phosphate and sulfate. *Am. J. Physiol.* **211**, 429–436 (1966).
21. Mosser, R., Reddy, M. C. M., Bruning, J. B., Sacchetti, J. C. & Reinhart, G. D. Redefining the role of the quaternary shift in *Bacillus stearothermophilus* phosphofructokinase. *Biochemistry* **52**, 5421–5429 (2013).
22. Jin, M. et al. Glycolytic enzymes coalesce in G bodies under hypoxic stress. *Cell Rep.* **20**, 895–908 (2017).
23. Adams, A. G., Bulusu, R. K. M., Mukhitov, N., Mendoza-Cortes, J. L. & Roper, M. G. Online measurement of glucose consumption from HepG2 cells using an integrated bioreactor and enzymatic assay. *Anal. Chem.* **91**, 5184–5190 (2019).
24. Santamaria, B., Estevez, A. M., Martinez-Costa, O. H. & Aragon, J. J. Creation of an allosteric phosphofructokinase starting with a non-allosteric enzyme. The case of dictyostelium discoideum phosphofructokinase. *J. Biol. Chem.* **277**, 1210–1216 (2002).
25. Huang, J. et al. CHARMM36m: an improved force field for folded and intrinsically disordered proteins. *Nat. Methods* **14**, 71–73 (2017).
26. Yao, X.-Q. et al. Dynamic coupling and allosteric networks in the alpha subunit of heterotrimeric G proteins. *Biophys. J.* **110**, 427a (2016).
27. Yugi, K. et al. Reconstruction of insulin signal flow from phosphoproteome and metabolome data. *Cell Rep.* **8**, 1171–1183 (2014).
28. Lynch, E. M., Kollman, J. M. & Webb, B. A. Filament formation by metabolic enzymes—A new twist on regulation. *Curr. Opin. Cell Biol.* **66**, 28–33 (2020).
29. Simonet, J. C., Burrell, A. L., Kollman, J. M. & Peterson, J. R. Freedom of assembly: metabolic enzymes come together. *Mol. Biol. Cell* **31**, 1201–1205 (2020).
30. Hvorecny, K. L. & Kollman, J. M. Greater than the sum of parts: mechanisms of metabolic regulation by enzyme filaments. *Curr. Opin. Struct. Biol.* **79**, 102530 (2023).
31. Garcia-Seisdedos, H., Empereur-Mot, C., Elad, N. & Levy, E. D. Proteins evolve on the edge of supramolecular self-assembly. *Nature* **548**, 244–247 (2017).
32. Seisdedos, H. G., Levin, T., Shapira, G., Freud, S. & Levy, E. D. Mutant libraries reveal negative design shielding proteins from supramolecular self-assembly and relocalization in cells. *Proc. Natl Acad. Sci. USA* **119** <https://doi.org/10.1073/pnas.2101171119> (2022).
33. Lynch, E. M. & Kollman, J. M. Coupled structural transitions enable highly cooperative regulation of human CTPS2 filaments. *Nat. Struct. Mol. Biol.* **27**, 42–48 (2020).
34. Lynch, E. M. et al. Human CTP synthase filament structure reveals the active enzyme conformation. *Nat. Struct. Mol. Biol.* **24**, 507–514 (2017).
35. Barry, R. M. et al. Large-scale filament formation inhibits the activity of CTP synthetase. *eLife* **3**, e03638 (2014).
36. Stoddard, P. R. et al. Polymerization in the actin ATPase clan regulates hexokinase activity in yeast. *Science* **367**, 1039–1042 (2020).
37. Hunkeler, M. et al. Structural basis for regulation of human acetyl-CoA carboxylase. *Nature* **558**, 470–474 (2018).
38. Pony, P., Rapisarda, C., Terradot, L., Marza, E. & Fronzes, R. Filamentation of the bacterial bi-functional alcohol/aldehyde dehydrogenase AdhE is essential for substrate channeling and enzymatic regulation. *Nat. Commun.* **11**, 1426 (2020).
39. Kim, G. et al. Aldehyde-alcohol dehydrogenase undergoes structural transition to form extended spiroosomes for substrate channeling. *Commun. Biol.* **3**, 298 (2020).
40. Hu, H.-H. et al. Filamentation modulates allosteric regulation of PRPS. *eLife* **11**, e79552 (2022).
41. Burrell, A. L. et al. IMPDH1 retinal variants control filament architecture to tune allosteric regulation. *Nat. Struct. Mol. Biol.* **29**, 47–58 (2022).
42. Johnson, M. C. & Kollman, J. M. Cryo-EM structures demonstrate human IMPDH2 filament assembly tunes allosteric regulation. *eLife* **9**, e53243 (2020).
43. Hvorecny, K. L., Hargett, K., Quispe, J. D. & Kollman, J. M. Human PRPS1 filaments stabilize allosteric sites to regulate activity. *Nat. Struct. Mol. Biol.* **30**, 391–402 (2023).
44. Jang, S. et al. Glycolytic enzymes localize to synapses under energy stress to support synaptic function. *Neuron* **90**, 278–291 (2016).
45. Kohnhorst, C. L. et al. Identification of a multienzyme complex for glucose metabolism in living cells. *J. Biol. Chem.* **292**, 9191–9203 (2017).
46. Brüser, A., Kirchberger, J., Kloos, M., Sträter, N. & Schöneberg, T. Functional linkage of adenine nucleotide binding sites in mammalian muscle 6-phosphofructokinase. *J. Biol. Chem.* **287**, 17546–17553 (2012).
47. Suloway, C. et al. Automated molecular microscopy: the new Legoin system. *J. Struct. Biol.* **151**, 41–60 (2005).
48. Vallat, R. Pingouin: statistics in Python. *J. Open Source Softw.* **3**, 1026 (2018).
49. Punjani, A., Rubinstein, J. L., Fleet, D. J. & Brubaker, M. A. cryoSPARC: algorithms for rapid unsupervised cryo-EM structure determination. *Nat. Methods* **14**, 290–296 (2017).
50. Adams, P. D. et al. PHENIX: a comprehensive Python-based system for macromolecular structure solution. *Acta Crystallogr. D. Biol. Crystallogr.* **66**, 213–221 (2010).
51. Croll, T. I. ISOLDE: a physically realistic environment for model building into low-resolution electron-density maps. *Acta Crystallogr. D. Struct. Biol.* **74**, 519–530 (2018).
52. Pettersen, E. F. et al. UCSF Chimera—a visualization system for exploratory research and analysis. *J. Comput. Chem.* **25**, 1605–1612 (2004).
53. Young, G. et al. Quantitative mass imaging of single biological macromolecules. *Science* **360**, 423–427 (2018).
54. Voronkova, M. A. et al. Cancer-associated somatic mutations in human phosphofructokinase-1 reveal a critical electrostatic interaction for allosteric regulation of enzyme activity. *Biochem. J.* **480**, 1411–1427 (2023).
55. The PyMOL molecular graphics system, Version 2.5.4 Schrödinger, LLC. <https://www.pymol.org/> (2022).
56. Abraham, M. J. et al. GROMACS: High performance molecular simulations through multi-level parallelism from laptops to supercomputers. *SoftwareX* **1–2**, 19–25 (2015).
57. Jo, S., Kim, T., Iyer, V. G. & Im, W. CHARMM-GUI: a web-based graphical user interface for CHARMM. *J. Comput. Chem.* **29**, 1859–1865 (2008).
58. Kim, S. et al. CHARMM-GUI ligand reader and modeler for CHARMM force field generation of small molecules. *J. Comput. Chem.* **38**, 1879–1886 (2017).

59. Vanommeslaeghe, K. et al. CHARMM general force field: A force field for drug-like molecules compatible with the CHARMM all-atom additive biological force fields. *J. Comput. Chem.* **31**, 671–690 (2010).
60. Jorgensen, W. L., Chandrasekhar, J., Madura, J. D., Impey, R. W. & Klein, M. L. Comparison of simple potential functions for simulating liquid water. *J. Chem. Phys.* **79**, 926–935 (1983).
61. Feenstra, K. A., Hess, B. & Berendsen, H. J. C. Improving efficiency of large time-scale molecular dynamics simulations of hydrogen-rich systems. *J. Comput. Chem.* **20**, 786–798 (1999).
62. Darden, T., York, D. & Pedersen, L. Particle mesh Ewald: an N-log(N) method for Ewald sums in large systems. *J. Chem. Phys.* **98**, 10089–10092 (1993).
63. Hockney, R. W., Goel, S. P. & Eastwood, J. W. Quiet high-resolution computer models of a plasma. *J. Comput. Phys.* **14**, 148–158 (1974).
64. Hess, B., Bekker, H., Berendsen, H. J. C. & Fraaije, J. G. E. M. LINCS: a linear constraint solver for molecular simulations. *J. Comput. Chem.* **18**, 1463–1472 (1997).
65. Miyamoto, S. & Kollman, P. A. Settle: an analytical version of the SHAKE and RATTLE algorithm for rigid water models. *J. Comput. Chem.* **13**, 952–962 (1992).
66. Berendsen, H. J. C., van Postma, J., Van Gunsteren, W. F., DiNola, A. & Haak, J. R. Molecular dynamics with coupling to an external bath. *J. Chem. Phys.* **81**, 3684–3690 (1984).
67. Bussi, G., Donadio, D. & Parrinello, M. Canonical sampling through velocity rescaling. *J. Chem. Phys.* **126**, 014101 (2007).
68. Parrinello, M. & Rahman, A. Polymorphic transitions in single crystals: a new molecular dynamics method. *J. Appl. Phys.* **52**, 7182–7190 (1981).
69. Michaud-Agrawal, N., Denning, E. J., Woolf, T. B. & Beckstein, O. MDAAnalysis: a toolkit for the analysis of molecular dynamics simulations. *J. Comput. Chem.* **32**, 2319–2327 (2011).
70. Grant, B. J., Skjaerven, L. & Yao, X.-Q. The Bio3D packages for structural bioinformatics. *Protein Sci.* **30**, 20–30 (2021).
71. Humphrey, W., Dalke, A. & Schulten, K. VMD: visual molecular dynamics. *J. Mol. Graph.* **14**, 33–38 (1996). 27–8.

Acknowledgements

We are grateful to the Arnold and Mabel Beckman Cryo-EM Center at the University of Washington for the use of electron microscopes. This work was supported by the National Institutes of Health (1R35GM149542 and S10OD023476 to J.M.K.). S.T. was supported by the Czech Science Foundation (grant no. 23-06437S). B.A.W. was supported by West Virginia University Start-up funding and Visual Sciences CoBRE project leader funding (P2OGM144230). The authors would like to thank Ms. Katelyn Frock for her technical assistance.

Author contributions

E.M.L., H.H., L.S., M.C., S.T., and B.A.W. performed experiments and analyzed data. E.M.L., L.S., S.T., B.A.W., and J.M.K. prepared and edited the manuscript. S.T., B.A.W., and J.M.K. supervised the work.

Competing interests

The authors declare no competing interests.

Additional information

Supplementary information The online version contains supplementary material available at <https://doi.org/10.1038/s41467-024-51808-6>.

Correspondence and requests for materials should be addressed to Justin M. Kollman or Bradley A. Webb.

Peer review information *Nature Communications* thanks Lauren Albrecht and the other, anonymous, reviewers for their contribution to the peer review of this work. A peer review file is available.

Reprints and permissions information is available at <http://www.nature.com/reprints>

Publisher's note Springer Nature remains neutral with regard to jurisdictional claims in published maps and institutional affiliations.

Open Access This article is licensed under a Creative Commons Attribution-NonCommercial-NoDerivatives 4.0 International License, which permits any non-commercial use, sharing, distribution and reproduction in any medium or format, as long as you give appropriate credit to the original author(s) and the source, provide a link to the Creative Commons licence, and indicate if you modified the licensed material. You do not have permission under this licence to share adapted material derived from this article or parts of it. The images or other third party material in this article are included in the article's Creative Commons licence, unless indicated otherwise in a credit line to the material. If material is not included in the article's Creative Commons licence and your intended use is not permitted by statutory regulation or exceeds the permitted use, you will need to obtain permission directly from the copyright holder. To view a copy of this licence, visit <http://creativecommons.org/licenses/by-nc-nd/4.0/>.

© The Author(s) 2024